Article

Control and readout of a superconducting qubit using a photonic link

https://doi.org/10.1038/s41586-021-03268-x

Received: 3 August 2020

Accepted: 20 January 2021

Published online: 24 March 2021

Check for updates

F. Lecocq[1,2]✉, F. Quinlan[1]✉, K. Cicak[1], J. Aumentado[1], S. A. Diddams[1,2] & J. D. Teufel[1]✉

Delivering on the revolutionary promise of a universal quantum computer will require processors with millions of quantum bits (qubits)[1–3]. In superconducting quantum processors[4], each qubit is individually addressed with microwave signal lines that connect room-temperature electronics to the cryogenic environment of the quantum circuit. The complexity and heat load associated with the multiple coaxial lines per qubit limits the maximum possible size of a processor to a few thousand qubits[5]. Here we introduce a photonic link using an optical fibre to guide modulated laser light from room temperature to a cryogenic photodetector[6], capable of delivering shot-noise-limited microwave signals directly at millikelvin temperatures. By demonstrating high-fidelity control and readout of a superconducting qubit, we show that this photonic link can meet the stringent requirements of superconducting quantum information processing[7]. Leveraging the low thermal conductivity and large intrinsic bandwidth of optical fibre enables the efficient and massively multiplexed delivery of coherent microwave control pulses, providing a path towards a million-qubit universal quantum computer.

Superconducting circuits have emerged as a leading technology for quantum computing[8–10], thanks to steady progress in gate and measurement fidelity combined with the capability of lithographically producing large and complex qubit networks[11]. However, the demonstration of a complete architecture that can truly scale to millions of qubits remains an elusive milestone[5]. Indeed, such quantum processors must operate in a cryogenic environment to be superconducting and, more importantly, initialized close to their quantum ground state. As these processors operate at microwave frequencies on the order of 10 GHz, they require a temperature well below 100 mK to eliminate thermally activated transitions. This is achieved in commercial dilution refrigerators, whose base temperatures routinely reach below 20 mK. In current architectures, the superconducting qubits are controlled and measured with microwave pulses generated at room temperature and delivered via heavily attenuated coaxial lines; see Fig. 1a. Besides simple space limitations, this approach results in considerable heat loads as the number of qubits scales, both passive, due to the thermal conductivity of the coaxial lines, and also active, due to the signal power dissipated in the attenuators. This heat load competes against the limited cooling power of the cryostat, typically ~20 μW (ref. [5]). Therefore, with current technologies one could imagine systems with a few thousand qubits at best[5], far from the predicted numbers required for compelling applications of quantum computers[1–3].

These crucial challenges have motivated new approaches that seek to increase the possible size of superconducting quantum processors. The development of quantum coherent interconnects, which are capable of sharing fragile quantum states between processors in separate cryostats, has attracted much research attention but remains a long-standing challenge[12–16]. Concurrently, innovations in classical interconnects aim to reduce the heat load associated with interfacing with the quantum processor, taking the form of high-density wiring[17,18] or cryogenic electronics[19–23]. Indeed, even with successful quantum coherent interconnects, a scalable technology capable of delivering classical signals suitable for high-fidelity qubit operation could be instrumental in building a large-scale quantum computer.

Here, we use ubiquitous telecommunication technologies and standard radiofrequency–photonics components[24], designed for room-temperature operation (~300 K), to demonstrate an ultracryogenic photonic link (<100 mK). In this unexplored temperature regime, the photonic link exhibits noise levels approaching microwave vacuum fluctuations, enabling the control and measurement of highly coherent quantum states. In our approach, the microwave control signals are upconverted to the optical frequency domain using electro-optic modulators (EOMs), guided along optical fibres to the cryogenic environment of the processor and downconverted back to microwave frequencies using high-speed photodetection[6], see Fig. 1b. The vanishing thermal conductivity of optical fibres at low temperature and their large intrinsic bandwidth would enable the delivery of millions of control signals directly to the millikelvin stage with no substantial passive heat load. To evaluate this photonic link, we operate a commercial high-speed photodiode at 20 mK to control and measure a superconducting transmon qubit. We demonstrate the ability to perform high-fidelity single-shot qubit readout and fast qubit gates while maintaining quantum coherence. We then exploit the extreme noise sensitivity of the qubit to measure the photodiode noise at sub-microampere photocurrents, revealing shot-noise-limited performance. Finally, we consider the noise and heat dissipation of the photodiode together to predict the scalability of our approach, charting a path towards scaling well beyond the capability of traditional coaxial wiring.

[1]National Institute of Standards and Technology, Boulder, CO, USA. [2]Department of Physics, University of Colorado, Boulder, CO, USA. ✉e-mail: florent.lecocq@nist.gov; franklyn.quinlan@nist.gov; john.teufel@nist.gov

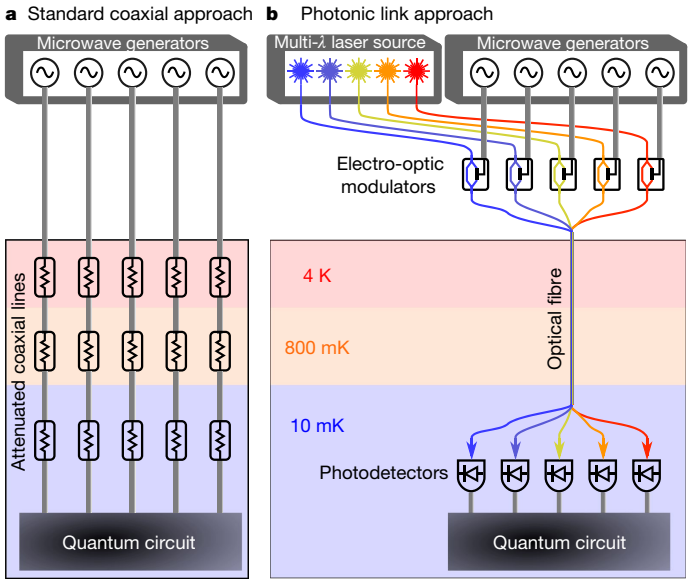

Fig. 1 | Photonic link concept. a, Schematic of a typical wiring approach with coaxial cabling. Room-temperature microwave signals are routed via heavily attenuated coaxial lines to a quantum circuit at the cold stage of a dilution refrigerator. The associated heat load consists of the passive load from thermal conductivity of the coaxial lines and the active load from the power dissipated in the attenuators. **b**, The photonic link approach. Room-temperature microwave signals are modulated onto an array of optical carriers and routed directly to high-speed photodetectors at the cold stage of the dilution refrigerator, using an optical fibre. The low thermal conductivity of silica suppresses the passive heat load, and the active heat load from optical power dissipation remains manageable.

The optical generation of microwave control signals relies on the photoelectric effect in a photodiode[25]. An incident optical photon generates an electron–hole pair in a semiconductor, with a quantum efficiency η. The carriers are then swept away to the electrodes of the diode owing to a built-in or applied voltage, creating a current pulse. Summing over many incident photons yields the photocurrent, $I = \mathcal{R}P_o$, where $\mathcal{R} = \eta e/\hbar\omega_o$ is the responsivity, e is the electron charge, P_o is the incident optical power, ω_o is the frequency of the optical photons, and $\hbar$ is the reduced Planck constant. Full-depth modulation of the optical power at a microwave (μ) frequency ω_μ that is well within the bandwidth of the photodiode results in an oscillating photocurrent at that same frequency, with an output microwave power $P_\mu = \frac{1}{2}Z\bar{I}^2$ where $\bar{I} = \langle I \rangle$ is the average photocurrent and Z is the impedance of the load.

The transmon qubit used in this work consists of a single Josephson junction shunted by a capacitor, forming an oscillator that is nonlinear at the single-photon level[4,26]. Full control over its quantum state $|\psi\rangle = \alpha|g\rangle + \beta|e\rangle$, where $|g\rangle$ and $|e\rangle$ are, respectively, the ground and first excited states, is achieved through coherent drives at the transition frequency ω_q. The qubit is dispersively coupled to a linear microwave cavity of linewidth κ such that the cavity resonance frequency depends on the qubit state, $\omega_{g,e} = \omega_c \pm \chi$, with ω_c the mean cavity resonance frequency and χ the dispersive shift (Methods). A drive at the mean cavity frequency is therefore reflected with a qubit-state-dependent phase shift $\pm 2\arctan(2\chi/\kappa)$, which is detected by a microwave homodyne set-up.

In this work we perform two separate experiments, in which we use a photonic link to generate microwave pulses that either readout (Fig. 2a–c) or control (Fig. 2d–f) a transmon qubit embedded in a three-dimensional microwave cavity[27]. A single antenna is used to address both the qubit and the cavity. Drives at $\omega_q/2\pi \approx 5.1$ GHz and $\omega_c/2\pi \approx 10.9$ GHz are physically separated by a microwave diplexer. The average qubit relaxation time is $T_1 \approx 43$ μs and the cavity linewidth is $\kappa/2\pi \approx 3$ MHz. The photonic link consists of a diode laser operating at a wavelength of 1,490 nm and a commercial EOM at room temperature, connected via an optical fibre to a InGaAs photodiode at 20 mK. For comparison, microwave signals can be routed to the quantum circuit with full vector control either through the photonic link or through a regular coaxial line. Detailed descriptions of the experimental set-ups are available in Methods and Table 1.

In the first experiment, signals generated by the photodiode drive the microwave cavity—see Fig. 2a. The laser power is suppressed during the qubit state manipulation, and then turned on and modulated at the cavity frequency ω_c to perform the readout. In Fig. 2b we drive the cavity into a coherent state of approximately 15 photons, using an average photocurrent $\bar{I} = 20$ nA during the measurement pulse. We show the histograms of 4×10^4 measurements of the homodyne signal, integrated over 400 ns, with the qubit initialized in the ground or excited state. We resolve two well separated Gaussian distributions corresponding to the ground and excited state of the qubit[28]. We extract a single-shot measurement fidelity of 98%, identical to the fidelity obtained using the regular coaxial line (not shown), and mainly limited by qubit decay during the measurement. To determine the effect that readout with a photonic link may have on qubit coherence, in Fig. 2c we compare the qubit coherence time T_2 when measured using the photodiode or the coaxial line. We show the ensemble average of two representative sets of 10^4 measurements as a function of the delay between two π/2 pulses, yielding Ramsey oscillations. In both cases we extract the same coherence time $T_2 = 37$ μs from the exponential decay of the oscillations. Additionally we do not see any indication that the qubit relaxation rate is degraded by stray optical light (see Methods and Extended Data Fig. 1).

In the second experiment, signals generated by the photodiode drive the qubit—see Fig. 2d. The laser power is modulated at the qubit frequency ω_q to control the qubit state, followed by a readout pulse at the cavity frequency using a coaxial line. When driven on resonance, the qubit undergoes Rabi oscillations between its ground and excited states at a frequency Ω_R, shown in Fig. 2e as a function of the amplitude of the drive at the cavity, using either the photodiode or a regular coaxial line. The corresponding average photocurrent is shown on the upper axis. For Rabi frequencies much less than the transmon's anharmonicity, $\delta/2\pi = 210$ MHz, the transmon is well approximated by a two-level system, and the Rabi frequency increases linearly with the drive amplitude. At higher drive power, the Rabi frequency deviates from the linear scaling, as expected from multilevel dynamics[29]. We note that precise matching of the Rabi rates of the photonic link to the coaxial line drive is achieved without any signal predistortion to compensate for nonlinearities of the photonic link. A typical Rabi oscillation driven by the photodiode is shown in Fig. 2f, with $\Omega_R/2\pi = 44$ MHz and $\bar{I} = 4$ μA. High qubit gate fidelity is expected as the Rabi rate exceeds the decay rate of the oscillations by more than three orders of magnitude.

Excess photocurrent noise could potentially limit qubit gate or readout fidelity. Predicting the effect of photocurrent noise requires its precise measurement in a temperature and photocurrent regime previously unexplored for high-speed photodiodes. Here, we exploit the qubit–cavity system as a quantum spectrum analyser to measure the noise performance of the photodiode with excellent sensitivity. In the absence of technical noise, the photocurrent noise is fundamentally limited by shot noise[25], with a power spectral density given by $S_I = 2e\bar{I}$. This shot noise spectrum is white until the frequency cut-off of the photodiode, nominally 20 GHz. In each experiment the microwave diplexer ensures that the noise drives only either the cavity or the qubit into a thermal state. In Fig. 3a, photocurrent noise leads to an average cavity occupancy $\bar{n}$. Owing to the dispersive coupling, this results in a Stark shift of the qubit frequency as well as qubit dephasing[30–32], which we experimentally resolve by measuring Ramsey oscillations in the presence of a constant laser intensity. As expected with shot noise, the cavity occupancy increases linearly with photocurrent with an experimental background of about 1% (Methods). In Fig. 3b, photocurrent

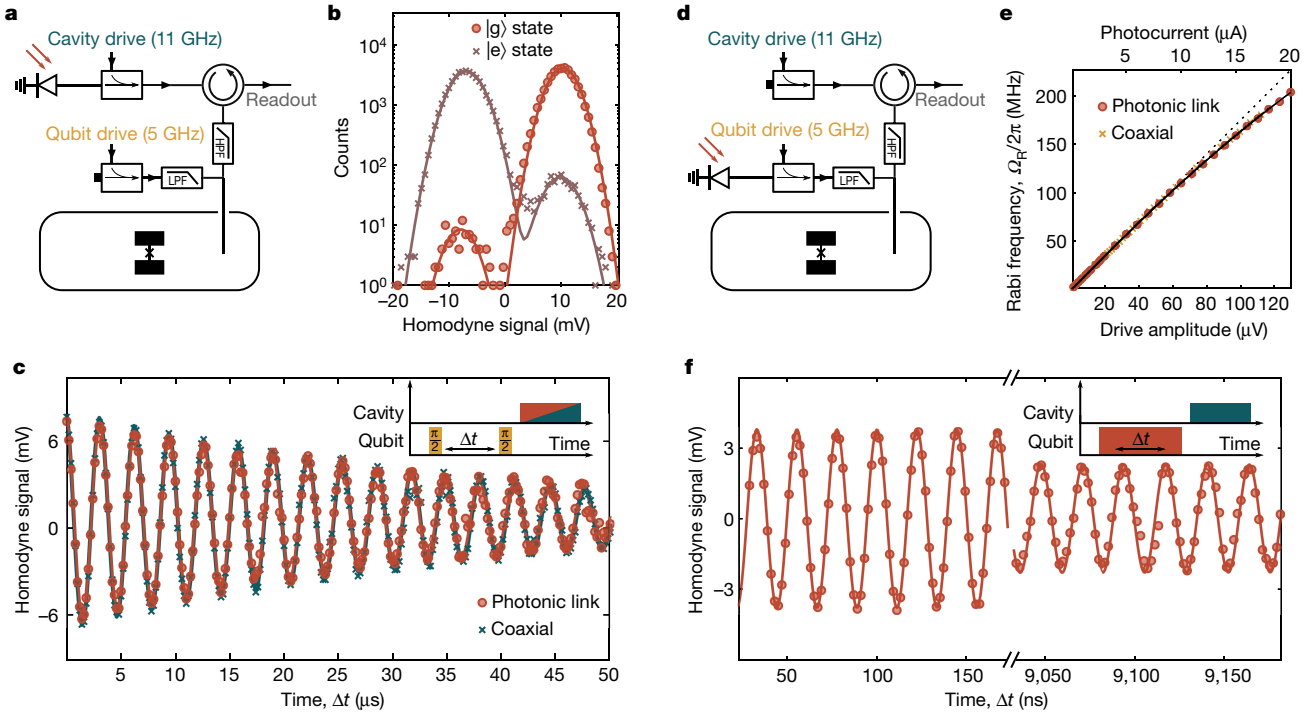

Fig. 2 | Qubit readout and control with a photonic link. a, Simplified experimental diagram for the qubit readout. A transmon qubit (frequency $\omega_q/2\pi = 5.1$ GHz) is dispersively coupled to a three-dimensional microwave cavity (frequency $\omega_c/2\pi = 10.9$ GHz). Whereas a single antenna is used to address both the qubit and the cavity, drives at ω_q and ω_c are physically separated by a microwave diplexer. Microwave signals generated by the photodetector are combined with the cavity drive, enabling the readout of the qubit using either the photonic link or a regular coaxial line. The reflected cavity drive acquires a qubit-state-dependent phase shift, measured by a high-efficiency homodyne detection set-up. **b**, Histogram of 4×10^4 measurements using a cavity drive generated by the photonic link, for the qubit prepared in its ground state (circles) or excited state (crosses). We extract a single-shot fidelity of 98% (400 ns integration time, average photocurrent $\bar{I} = 20$ nA). **c**, Representative qubit Ramsey oscillations measured using either the photonic link ($\bar{I} = 17.5$ nA) or the regular coaxial line, with the same decoherence time $T_2 = 37$ μs. **d**, Simplified experimental diagram for the qubit control. Compared to **a**, the microwave signals generated by the photodetector are now combined with the qubit drive, enabling the control of the qubit using either the photonic link or a regular coaxial line. **e**, Rabi frequency driven by the photonic link or the regular coaxial line, as a function of drive amplitude (amplitudes are referenced to the cavity antenna). The corresponding average photocurrent is shown on the upper *x* axis. The lines are the theoretical prediction for a two-level system (dashed line) or an anharmonic oscillator (solid line). **f**, Typical Rabi oscillation driven by the photonic link, with a Rabi rate more than three orders of magnitude faster than the decay rate of the oscillations ($\bar{I} = 4$ μA, $\Omega_R/2\pi = 44$ MHz). The lines in **b**, **c**, **f** are fits to the data. HPF, high-pass filter; LPF, low-pass filter.

noise leads to depopulation of the qubit ground state, extracted from the statistics of 10^4 projective single-shot measurements. The population of the excited states as a function of the photocurrent shows a linear behaviour, again in good agreement with shot noise, and a background qubit occupancy of about 10% (Methods). In Fig. 3c, we use the data in Fig. 3a, b, as well as independent calibration of the loss between the photodiode and the device for each experiment (see Methods), to refer the measured noise back to the output of the photodiode. The two datasets show excellent agreement with shot noise predictions, both in terms of the noise level and photocurrent dependence. In particular, we do not observe any major deviation from shot noise that could indicate, for example, excess optical intensity noise (proportional to $\bar{I}^2$), excess thermal noise due to local heating within the photodiode, or excess noise from the voltage noise at the microwave input of the EOM. At the photocurrents used for the qubit readout ($\bar{I} = 20$ nA) or control ($\bar{I} = 4$ μA), we infer that the optical shot noise will have negligible impact on measurement and gate fidelity (Methods).

After demonstrating that this photonic link meets the stringent requirements for the control and readout of a transmon qubit, we describe how this approach can scale to a large number of qubits. The number of qubits in a processor is limited by the heat load of the classical interconnects on the mixing chamber of the dilution refrigerator. We estimate the passive heat load of a typical optical fibre to be about 3 pW, allowing a typical dilution refrigerator with a cooling power of 20 μW at 20 mK to be wired with millions of optical fibres. In addition, each optical fibre has the bandwidth to easily support hundreds of qubits[33]. With negligible passive heat load, the active heat load due to the dissipation of optical power during qubit gates becomes the limitation. The maximum number of qubits that can be supported by photonic links is therefore inversely proportional to the duty cycle at which each qubit is driven. In Fig. 4 we compare the total heat load of a photonic link to a 20 μW cooling power, yielding a maximum number of physical qubits as a function of duty cycle. We assume that each qubit is addressed by its own optical fibre and photodiode, and use typical values for Rabi rate, pulse shaping and coupling rate to the drive line (Methods). In comparison with the photonic link approach, the total heat load for a regular coaxial approach is dominated by the passive heat load, measured to be 13 nW per 0.086 inch (2.2 mm) diameter stainless steel coaxial cable[5]. Recent milestone experiments[9,10] have operated at duty cycle of the order of 1% or less, at which the total heat load using a photonic link can be greatly reduced compared to the coaxial approach. Although the duty cycle of a gate sequence must be maximized to avoid the deleterious effects of decoherence, the rate at which the sequence is repeated can be reduced without sacrificing fidelity. This could be advantageous for noisy intermediate-scale quantum computations (NISQ)[34], where operating at a smaller overall duty cycle would allow for an increase in the number of qubits that can be addressed using photonic links.

Beyond the NISQ era, fault-tolerant quantum computation with a million qubits will need to run continuously at the highest duty cycle allowed by the quantum and classical hardware, possibly for hours or days[2,3]. Building such a quantum processor will require both

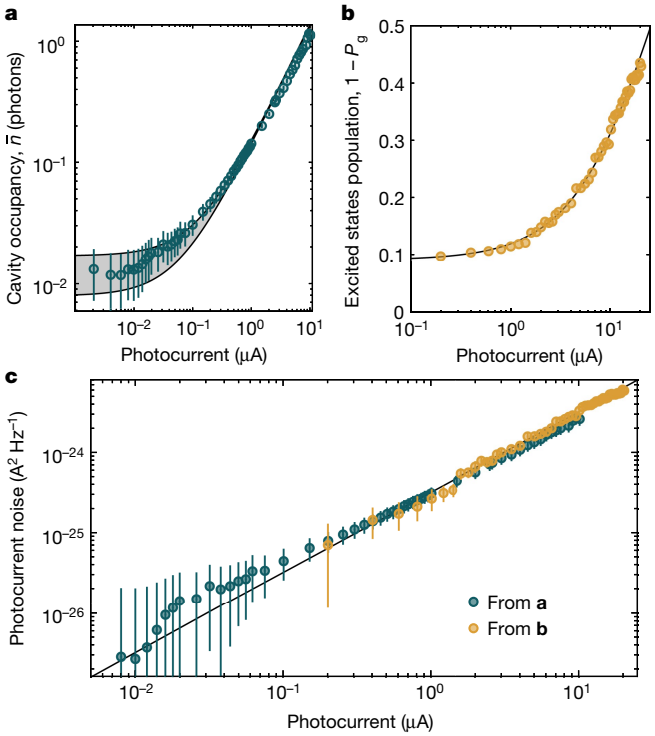

Fig. 3 | Photocurrent shot noise measurement. a, Average occupancy of the microwave cavity as a function of the average photocurrent, measured using the experimental set-up in Fig. 2a (dots). Lines are a theoretical prediction for background occupancy between 0.8% and 1.7%. **b**, Qubit excited-state population as a function of the average photocurrent, measured using the experimental set-up in Fig. 2d (dots). Lines are theoretical prediction. P_g, qubit ground-state population. **c**, Power spectral density of the photocurrent noise, referred to the output of the photodetector, as a function of the average photocurrent. Data are extracted from the cavity population in **a** (green dots) and the qubit population in **b** (yellow dots), and are in excellent agreement with the prediction from photocurrent shot noise (black line). All error bars represent 90% confidence intervals.

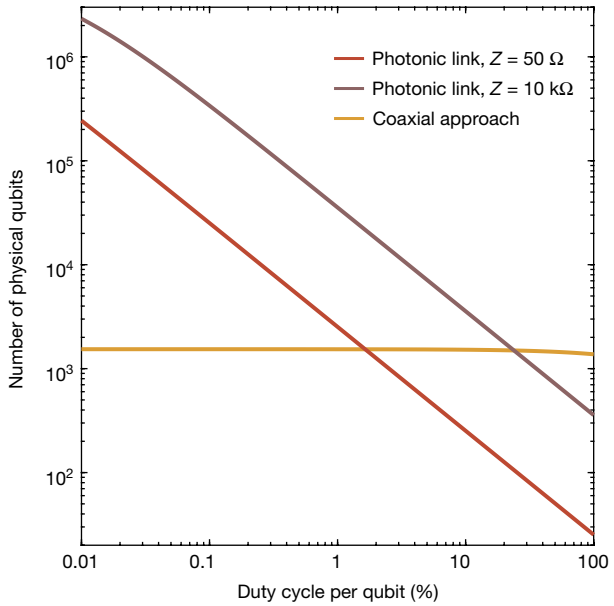

Fig. 4 | Qubit scaling comparison. Maximum number of qubits for a given cooling power, as a function of the duty cycle per qubit, for the typical coaxial approach, or using a photonic links with drive line impedance of either 50 Ω or 10 kΩ (see text). At low duty cycle, using a photonic link enables the control of a larger number of qubits owing to the absence of a passive heat load. Larger drive line impedance enables the reduction of the optical power necessary to deliver a given microwave power, reducing the heat load per qubit.

an improvement in cooling power and a reduction of the heat load. The coaxial approach would require a reduction of its passive heat load by orders of magnitude, and microwave multiplexing, thinner coaxial cables or superconducting ribbon cables[17,35] are currently being investigated. On the other hand, the photonic link approach would benefit from any reduction of its active heat load. As an example, the large source impedance of a photodiode can be exploited such that an increase in system impedance decreases the amount of photocurrent required to deliver a given amount of microwave power. This in turn reduces the required optical power to drive each qubit, leading to an increase in the maximum number of physical qubits (see Fig. 4), albeit at the possible expense of gate fidelity (Methods). Additionally, multiplexing schemes—such as encoding multiple microwave signals onto a single optical carrier or the use of short optical pulses—may likewise provide a path to reduce the required optical power even further.

In conclusion, we have experimentally demonstrated an ultracryogenic photonic link as a scalable platform for addressing superconducting qubits. By incorporating high-speed photodetection with a superconducting qubit at millikelvin temperatures, we have shown that the photonic link is fully compatible with quantum coherent qubit operation. Furthermore, we have in turn used the qubit to measure the noise of the photonic link and showed that the current noise is fundamentally set by the shot noise of the light, even at extremely low photocurrents. This work highlights the benefits of mature opto-electronic technology for quantum applications and will only be enhanced by further optimization of hardware and protocols specifically tailored for cryogenic operation. Combined with photonic methods for transmitting the qubit state information to room temperature on optical fibre[22,23], we envision a fully photonic interface with a superconducting quantum processor. This promising technology provides a path towards scaling superconducting quantum processors to an unprecedented number of quantum bits, enabling many of the longstanding promises of the quantum revolution.

Table 1 | Device parameters

Parameter	Symbol	Value
Qubit frequency in Figs. 2a–c,3a	ω_q	$\omega_q/2\pi$ = 5.052 GHz
Qubit frequency in Figs. 2d–f, 3b	ω_q	$\omega_q/2\pi$ = 5.088 GHz
Average qubit relaxation time	T_1	$T_1 \approx 43$ μs
Cavity frequency	ω_c	$\omega_c/2\pi$ = 10.866 GHz
Cavity linewidth	κ	$\kappa/2\pi$ = 3.09 MHz
Exchange coupling strength	g	$g/2\pi$ = 294 MHz
Dispersive shift	χ	$\chi/2\pi$ = 517 kHz
Transmon anharmonicity	δ	$\delta/2\pi$ = 210 MHz
Critical photon number	n_{crit}	n_{crit} = 98
Photodiode responsivity	R	R = 0.55 A W^{-1}

Online content

Any methods, additional references, Nature Research reporting summaries, source data, extended data, supplementary information, acknowledgements, peer review information; details of author contributions and competing interests; and statements of data and code availability are available at https://doi.org/10.1038/s41586-021-03268-x.

1. Fowler, A. G., Mariantoni, M., Martinis, J. M. & Cleland, A. N. Surface codes: towards practical large-scale quantum computation. *Phys. Rev. A* **86**, 032324 (2012).

2. Reiher, M., Wiebe, N., Svore, K. M., Wecker, D. & Troyer, M. Elucidating reaction mechanisms on quantum computers. *Proc. Natl Acad. Sci. USA* **114**, 7555–7560 (2017).
3. Gidney, C. & Ekerå, M. How to factor 2048 bit RSA integers in 8 hours using 20 million noisy qubits. Preprint at https://arxiv.org/abs/1905.09749 (2019).
4. Krantz, P. et al. A quantum engineer's guide to superconducting qubits. *Appl. Phys. Rev.* **6**, 021318 (2019).
5. Krinner, S. et al. Engineering cryogenic setups for 100-qubit scale superconducting circuit systems. *EPJ Quantum Technol.* **6**, 2 (2019).
6. Davila-Rodriguez, J. et al. High-speed photodetection and microwave generation in a sub-100-mK environment. In *2019 Conf. Lasers and Electro-Optics (CLEO)* SF2N.1 (2019)
7. Devoret, M. H. & Schoelkopf, R. J. Superconducting circuits for quantum information: an outlook. *Science* **339**, 1169–1174 (2013).
8. Ofek, N. et al. Extending the lifetime of a quantum bit with error correction in superconducting circuits. *Nature* **536**, 441–445 (2016).
9. Arute, F. et al. Quantum supremacy using a programmable superconducting processor. *Nature* **574**, 505–510 (2019).
10. Andersen, C. K. et al. Repeated quantum error detection in a surface code. *Nat. Phys.* **16**, 875–880 (2020).
11. Blais, A., Girvin, S. M. & Oliver, W. D. Quantum information processing and quantum optics with circuit quantum electrodynamics. *Nat. Phys.* **16**, 247–256 (2020).
12. Andrews, R. W. et al. Bidirectional and efficient conversion between microwave and optical light. *Nat. Phys.* **10**, 321–326 (2014).
13. Rueda, A. et al. Efficient microwave to optical photon conversion: an electro-optical realization. *Optica* **3**, 597–604 (2016).
14. Jiang, W. et al. Efficient bidirectional piezo-optomechanical transduction between microwave and optical frequency. *Nat. Commun.* **11**, 1166 (2020).
15. Mirhosseini, M., Sipahigil, A., Kalaee, M. & Painter, O. Superconducting qubit to optical photon transduction. *Nature* **588**, 599–603 (2020).
16. Magnard, P. et al. Microwave quantum link between superconducting circuits housed in spatially separated cryogenic systems. *Phys. Rev. Lett.* **125**, 260502 (2020).
17. Tuckerman, D. B. et al. Flexible superconducting Nb transmission lines on thin film polyimide for quantum computing applications. *Supercond. Sci. Technol.* **29**, 084007 (2016).
18. Smith, J. P. et al. Flexible coaxial ribbon cable for high-density superconducting microwave device arrays. *IEEE Trans. Appl. Supercond.* **31**, 2500105 (2021).
19. McDermott, R. et al. Quantum–classical interface based on single flux quantum digital logic. *Quantum Sci. Technol.* **3**, 024004 (2018).
20. Leonard, E. et al. Digital coherent control of a superconducting qubit. *Phys. Rev. Appl.* **11**, 014009 (2019).
21. Bardin, J. C. et al. Design and characterization of a 28-nm bulk-CMOS cryogenic quantum controller dissipating less than 2 mW at 3 K. *IEEE J. Solid-State Circuits* **54**, 3043–3060 (2019).
22. Youssefi, A. et al. Cryogenic electro-optic interconnect for superconducting devices. Preprint at https://arxiv.org/abs/2004.04705 (2020).
23. de Cea, M. et al. Photonic readout of superconducting nanowire single photon counting detectors. *Sci. Rep.* **10**, 9470 (2020).
24. Capmany, J. & Novak, D. Microwave photonics combines two worlds. *Nat. Photon.* **1**, 319–330 (2007).
25. Saleh, B. E. A. & Teich, M. C. *Fundamentals of Photonics* (Wiley-Interscience, 2007).
26. Koch, J. et al. Charge-insensitive qubit design derived from the Cooper pair box. *Phys. Rev. A* **76**, 042319 (2007).
27. Paik, H. et al. Observation of high coherence in Josephson junction qubits measured in a three-dimensional circuit QED architecture. *Phys. Rev. Lett.* **107**, 240501 (2011).
28. Walter, T. et al. Rapid high-fidelity single-shot dispersive readout of superconducting qubits. *Phys. Rev. Appl.* **7**, 054020 (2017).
29. Claudon, J., Balestro, F., Hekking, F. W. J. & Buisson, O. Coherent oscillations in a superconducting multilevel quantum system. *Phys. Rev. Lett.* **93**, 187003 (2004).
30. Schuster, D. I. et al. a.c. Stark shift and dephasing of a superconducting qubit strongly coupled to a cavity field. *Phys. Rev. Lett.* **94**, 123602 (2005).
31. Gambetta, J. et al. Qubit–photon interactions in a cavity: measurement-induced dephasing and number splitting. *Phys. Rev. A* **74**, 042318 (2006).
32. Yan, F. et al. The flux qubit revisited to enhance coherence and reproducibility. *Nat. Commun.* **7**, 12964 (2016).
33. Winzer, P. J., Neilson, D. T. & Chraplyvy, A. R. Fiber-optic transmission and networking: the previous 20 and the next 20 years. *Opt. Express* **26**, 24190–24239 (2018).
34. Preskill, J. Quantum computing in the NISQ era and beyond. *Quantum* **2**, 79 (2018).
35. Smith, T. L., Anthony, P. J. & Anderson, A. C. Effect of neutron irradiation on the density of low-energy excitations in vitreous silica. *Phys. Rev. B* **17**, 4997 (1978).

Methods

Primer on circuit quantum electrodynamics

Here we briefly review the basic theory for the transmon/cavity system, introducing all the notation and assumptions used in this work. More detail can be found in refs. [4,28], and a list of parameters is shown in Table 1.

The transmon is an anharmonic oscillator of frequency ω_q and anharmonicity δ. To a good approximation the transmon can be treated as a two-level system, forming the qubit. It is coupled to a resonant cavity of frequency ω_c via the Jaynes–Cummings Hamiltonian,

$$\mathcal{H}_{qed} = \frac{1}{2}\hbar\omega_q\hat{\sigma}_z + \hbar\omega_c\hat{a}^\dagger\hat{a} + \hbar g(\hat{a}\hat{\sigma}_+ + \hat{a}^\dagger\hat{\sigma}_-), \quad (1)$$

where g is the strength of the exchange interaction, $\hat{\sigma}_\pm = (\hat{\sigma}_x \pm i\hat{\sigma}_y)/2$ (where $\hat{\sigma}_{x,y,z}$ are the Pauli qubit operators), and $\hat{a}$ and $\hat{a}^\dagger$ are the cavity creation and annihilation operators, respectively. We operate in the dispersive regime, where the detuning between the qubit and cavity frequencies is large compared to the coupling strength, $|\Delta| = |\omega_c - \omega_q| \gg g$, preventing any direct energy exchange between the two systems. In this regime, the Hamiltonian becomes

$$\mathcal{H}_{qed} \approx \frac{1}{2}\hbar\omega_q\hat{\sigma}_z + \hbar\omega_c\hat{a}^\dagger\hat{a} - \chi\hat{\sigma}_z\hat{a}^\dagger\hat{a}, \quad (2)$$

where $\chi = g^2/\Delta$ is the so-called dispersive shift. The cavity resonance frequency depends on the qubit state: $\omega_c + \chi$ or $\omega_c - \chi$ for the qubit in, respectively, the ground state, $|g\rangle$, or excited state, $|e\rangle$. Conversely the qubit frequency is shifted by 2χ per photon in the cavity and we redefined the qubit frequency as $\omega_q \equiv \omega_q + \chi$ to absorb the Lamb shift. Importantly, the dispersive approximation is only valid for small photon numbers in the cavity, and spurious qubit transitions occur when approaching the critical photon number $n_{crit} = \Delta^2/4g^2$. Finally, taking into account the higher levels of the transmon modifies the expression for the dispersive shift, $\chi = \frac{g^2}{\Delta}\frac{\delta}{\Delta+\delta}$, and renormalizes slightly the qubit and cavity frequencies[26].

In our system the cavity and the qubit are coupled to the environment using a single antenna. The cavity linewidth κ is dominated by the coupling to the antenna. Owing to the filtering of the cavity, the qubit is only weakly coupled to the antenna, at a rate Γ_{ext}, much smaller than the intrinsic relaxation rate Γ_{int} of the qubit.

Qubit readout. The qubit is read out by driving the cavity with an input microwave field of amplitude α_{in} and frequency ω_d. In the steady state, the resulting coherent state, $\alpha_{g,e}$, depends on the qubit state $|g\rangle$ or $|e\rangle$, following the equation of motion:

$$(\omega_d - \omega_c \mp \chi + i\kappa/2)\alpha_{g,e} = i\sqrt{\kappa}\,\alpha_{in}. \quad (3)$$

The output field, $\alpha_{out} = \sqrt{\kappa}\alpha_{g,e} - \alpha_{in}$, acquires a qubit-state-dependent phase shift that enables qubit-state discrimination. One can show that the measurement rate is $\Gamma_m = \kappa|\alpha_e - \alpha_g|^2$ and is maximized by the distance in phase space between the two coherent states[36]. The qubit measurement fidelity is defined as $F = 1 - P(e|g) - P(g|e)$, where $P(x|y)$ is the probability of measuring the qubit state x when prepared in the state y. In absence of preparation errors and qubit transitions during the measurement, and in the steady state, the measurement fidelity after an integration time τ can be written as $F = \mathrm{erf}(\sqrt{\eta\tau\Gamma_m/2})$, where η is the microwave measurement efficiency[28], and erf denotes the error function.

Photon number fluctuations and qubit dephasing. Fluctuations of the number of photons in the cavity induce fluctuations of the qubit frequency and therefore dephasing. The Stark shift and dephasing rate for an average thermal occupancy of the cavity $\bar{n}$ are, respectively,

$$\Delta_{Stark}^{th} = \beta 2\chi\bar{n},$$
$$\Gamma_\phi^{th} = \beta\frac{4\chi^2}{\kappa}\bar{n}, \quad (4)$$

where $\beta = \kappa^2/(\kappa^2 + 4\chi^2)$. Note that these expressions are only valid for $\bar{n} \ll 1$ and more general forms can be found in ref. [37].

Experimentally, we extract the Stark shift from the frequency of Ramsey oscillations. The qubit dephasing is extracted from the exponential decay of the Ramsey oscillations, $\Gamma_2 = \Gamma_1/2 + \Gamma_\phi$, and we assume it is dominated by photon number fluctuations, $\Gamma_\phi = \Gamma_\phi^{th}$. The cavity occupancy in Fig. 3a is extracted from the measurement of the Stark shift.

Qubit control. Under resonant drive, the qubit undergoes Rabi oscillations between the ground and excited states at the Rabi rate $\Omega_R = 2\sqrt{\dot{n}\Gamma_{ext}}$ where $\dot{n}$ is the number of photons per second at the antenna. When the Rabi rate approaches the transmon anharmonicity, $\Omega_R \approx \delta$, the transmon dynamics involve higher excited states, leaving the computational subspace. A hallmark of this regime is the deviation from the linear relation between Rabi rate and drive amplitude[29], as observed in Fig. 2e. In practice, typical superconducting quantum processors operate in the linear regime, $\Omega_R < \delta/2$.

Primer on photodetection

Here we briefly explain the basic principle of a photodiode, introducing all the notation and assumptions used in this work. More detail can be found in ref. [25].

Photocurrent. The photodiode can be seen as a high impedance current source, with an output current I proportional to the incident optical power P_o such that $I = \mathcal{R}P_o$, where $\mathcal{R} = \eta e/\hbar\omega_o$ is the responsivity, e is the electron charge, ω_o is the frequency of the optical photons and η is the quantum efficiency (defined as the probability of generating an electron-hole pair per incident photon). A perfectly efficient photodiode ($\eta = 1$) operating at a wavelength of 1,490 nm ($\omega_o/2\pi \approx$ 201 THz) has a maximum responsivity $\mathcal{R} \approx 1.2$ A W^{-1}. In practice, the quantum efficiency depends on extrinsic effects such as alignment and Fresnel reflections, and on the intrinsic efficiency of the detector. For the photodiode used in this work, we measure a responsivity of 0.7 A W^{-1} at room temperature. At 20 mK the responsivity drops to 0.5 A W^{-1}, probably caused by a change of the optical alignment owing to thermal contractions.

Microwave generation. Microwaves are generated by modulating the optical power such that $P_o(t) = \bar{P}_o(1 + m\cos(\omega t + \theta))$ where $\bar{P}_o$ is the average optical power, m is the modulation depth ($m \le 1$), ω is the modulation frequency, and θ is the modulation phase. This induces an oscillating photocurrent $I(t) = h(t) * \mathcal{R}P_o(t)$ where $h(t)$ is the impulse response of the photodiode and $*$ denotes convolution. The amplitude and phase of the modulation are preserved, enabling vector control of the resulting microwave signal. The corresponding microwave power P_μ in a load impedance Z is $P_\mu = \frac{1}{2}m^2\bar{I}^2 \times |H(\omega)|^2 \times Z$, where $\bar{I} = \mathcal{R}\bar{P}_o$ is the average photocurrent and $H(\omega)$ is the transfer function of the photodiode.

Photodiode bandwidth. For the photodiode used here, the response function is limited by the resistor–capacitor (RC) time constant, with a 3-dB cut-off frequency $f_{3dB} \approx 20$ GHz set by the capacitance of the diode ($C_d \approx 150$ fF) and the impedance of the load ($Z = 50\ \Omega$). If the load impedance increased to $Z = 10$ kΩ and the capacitance remained unchanged, this cut-off would be reduced to $f_{3dB} \approx 100$ MHz. Crucially, however, driving a qubit or a cavity does not require a matched source. The important parameter is the real part of the admittance of the source, $\mathrm{Re}[Y(\omega)]$, near the qubit resonance frequency[38,39]. Typically, a transmon

qubit is connected to a 50-Ω source via a small coupling capacitor C_c, ensuring Re[$Y(\omega)$] does not appreciably damp the qubit and is roughly constant over the bandwidth needed for fast pulses. Specifically, for driving a 6-GHz transmon qubit with total capacitance of $C_q \approx 100$ fF, a coupling capacitor of $C_c \approx 35$ aF would give a coupling of $\Gamma_{ext}^{-1} = 1$ ms. If using a source with a complex impedance (such as a realistic diode with its intrinsic capacitance), one can choose a different coupling capacitor that will achieve the same Re[$Y(\omega)$] at the qubit frequency. For a diode with $Z = 10$ kΩ and $C_d = 150$ fF, $C_c = 150$ aF achieves the same coupling $\Gamma_{ext}^{-1} = 1$ ms, with a fractional variation of Re[$Y(\omega)$] of 10^{-4} over 1 GHz of bandwidth. This analysis assumes that the electrical length of the transmission line between the high-impedance diode and the qubit is small (≪1 cm). As the line impedance will be much lower than 10 kΩ, longer connections would require precise control of the electrical length to avoid standing wave resonances.

Photocurrent shot noise. The probabilistic nature of creating electron–hole pairs results in photocurrent shot noise with power spectral density[40] $S_I(\omega) = 2e\bar{I}|H(\omega)|^2$.

Other definitions and notation. In the main text we assume $m = 1$ and $|H(\omega)| = 1$. We define the microwave photon flux $\dot{n} = P_\mu/\hbar\omega$ as the number of photons per second and the microwave photon noise spectral density $\bar{n} = S_I Z/\hbar\omega$ as the number of photons per second per hertz. Because it simplifies notation, it is convenient to define $\Lambda = \hbar\omega/Z$, in units of J Ω^{-1}.

Excess photocurrent noise

Although the photocurrent noise measurements in Fig. 3 are consistent with shot-noise-limited photodetection for photocurrents up to 20 μA, we estimate here the possible contributions of two other known sources of excess photocurrent noise: voltage noise at the microwave input of the electro-optic intensity modulator and excess laser intensity noise.

Voltage noise at the EOM input. We consider a lossless EOM with an infinite extinction ratio. The output optical power is $P_o(t) = \bar{P}_o(1 + \sin(\pi V(t)/V_\pi))$ where V_π is the voltage required to go from maximum transmission to minimum transmission and $V(t) = V_\mu(t) + V_{dc}$ is the input voltage. For a modulator biased at quadrature ($V_{dc} = 0$) and in the limit of small input voltage ($V_\mu(t) \ll V_\pi$) the output power becomes $P_o(t) = \bar{P}_o(1 + \pi V_\mu(t)/V_\pi)$. The noise variance of the optical power is then $\langle \delta P_o^2 \rangle = \bar{P}_o{}^2 \pi^2 \langle \delta V_\mu^2 \rangle / V_\pi^2$ where the angle brackets denote the ensemble average. The photocurrent noise variance is then $\langle \delta I^2 \rangle = \mathcal{R}^2 \langle \delta P_o^2 \rangle = \bar{I}^2 \pi^2 \langle \delta V_\mu^2 \rangle / V_\pi^2$. In terms of the current noise power spectral density, this becomes $S_I^{\delta V}(\omega) = S_V(\omega)\bar{I}^2\pi^2/V_\pi^2$ where $S_V(\omega) = 4k_B T_N Z_{EOM}$ (k_B, Boltzmann constant) is the input voltage noise power spectral density set by the noise temperature T_N of the input impedance of the EOM, Z_{EOM}.

Excess laser noise. Laser intensity noise is usually given as a fractional variation, termed relative intensity noise (RIN), defined as $\mathrm{RIN}(\omega) = S_P(\omega)/P_o^2$ where $S_P(\omega)$ is the power spectral density of the optical power fluctuations[41], in units of W^2 Hz^{-1}. The linear relationship between optical power and photocurrent leads to a photocurrent noise due to RIN given by $S_I^{RIN}(\omega) = \bar{I}^2 \mathrm{RIN}(\omega)$.

Total photocurrent noise. The total current noise emitted by the photodiode is then $S_I(\omega) = 2e\bar{I} + S_I^{\delta V}(\omega) + S_I^{RIN}(\omega)$. At the highest photocurrent used in this work, $\bar{I} = 20$ μA, the photocurrent shot noise is $2e\bar{I} \approx 8 \times 10^{-24}$ A^2 Hz^{-1}. For the voltage noise on the EOM, we measure $V_\pi = 3.5$ V and $T_N = 2.5 \times 10^5$ K, set by a power amplifier at the input of the EOM. This yields $S_I^{\delta V}(\omega) \approx 3 \times 10^{-25}$ A^2 Hz^{-1}, more than an order of magnitude smaller than the photocurrent shot noise. The RIN of readily available commercial semiconductor distributed feedback (DFB) lasers is below 10^{-14} Hz^{-1}, and can approach 10^{-16} Hz^{-1}, leading to a current noise $S_I^{RIN} < 5 \times 10^{-24}$ A^2 Hz^{-1} . As we do not resolve experimentally any deviation from photocurrent shot noise, we conclude that the laser RIN is below 10^{-15} Hz^{-1}.

Finally, we emphasize that our measurement is sensitive only to noise above microwave vacuum fluctuations and that any residual thermal noise is already included in the qubit Stark shift or qubit population at zero photocurrent.

Attenuation between the cavity antenna and photodiode

Here we discuss the procedure to move the reference plane from the cavity antenna to the photodiode. As the hardware and frequencies differ slightly between the qubit control and readout experiments, they require separate in situ calibrations.

Qubit control. We start by calibrating the microwave power at the cavity antenna using the coaxial line. From the measurement of the power at room temperature and the calibration of the attenuation from room temperature to the cavity antenna we can calibrate the x axis in Fig. 2e. We then compare to the Rabi rate to extract the coupling rate between the qubit and cavity antenna, $1/\Gamma_{ext} = 198$ μs. We define the loss between the photodiode and the cavity antenna, A, so that the power at the cavity antenna is $AP_\mu = A\frac{1}{2}Z\bar{I}^2$, where A includes the effect of explicit loss and the response function of the photodiode. Comparing the Rabi rate to the average photocurrent, we find $A = 0.034$. We then extract the current noise spectral density of the photocurrent, S_I, using the qubit ground-state population P_g measured in Fig. 3b. From detailed balance we find $(\Gamma_{int} + \Gamma_{ext})n = \Gamma_{int} n_{int} + \Gamma_{ext} n_{ext}$ where $n = (1 - P_g)/P_g$, n_{int} is the average photon number in the internal bath extracted from the equilibrium population at zero photocurrent, and $n_{ext} = AZS_I/\hbar\omega_q$. Finally we get:

$$S_I = \frac{\hbar\omega_q}{AZ\Gamma_{ext}}[(\Gamma_{int} + \Gamma_{ext})n - \Gamma_{int} n_{int}]. \quad (5)$$

Qubit readout. We fix the photocurrent and use the Stark shift to calibrate the intra-cavity photon number[30,36] and therefore extract the power at the cavity antenna $AP_\mu = A\frac{1}{2}Z\bar{I}^2$. We find $A = 0.065$. As the measurement cavity is overcoupled, we can simply extract the current noise spectral density of the photocurrent from the cavity occupancy, $S_I = n\hbar\omega_c/AZ$.

Effect of photocurrent shot noise on measurement fidelity and gate errors

In this section we discuss the effect of the microwave noise induced by the photocurrent shot noise of the photodiode. In the context of qubit readout, extraneous noise at the cavity frequency (1) dephases the qubits coupled to it and (2) reduces the microwave measurement efficiency, which in turn impacts the qubit measurement fidelity. In the context of qubit control, extraneous noise at the qubit frequency induces transitions to the excited states which reduces gate fidelity. To simplify the discussion, we consider a photodiode with unity quantum efficiency and operating well within its bandwidth, and neglect loss between the photodiode and the cavity or the qubit control line.

Qubit readout. Optimal measurement speed and separation in phase space between α_g and α_e is obtained for $2\chi = \kappa$ and $\omega_d = \omega_c$ (refs. [4,28]), leading to $|\alpha_g|^2 = |\alpha_e|^2 = |\alpha|^2 = 2\dot{n}/\kappa$. The corresponding average photocurrent is $\bar{I} = \sqrt{\kappa\Lambda}\,|\alpha|$. In turn the microwave noise is $\bar{n} = 2e\sqrt{\kappa/\Lambda}\,|\alpha|$, which induces qubit dephasing according to equation (4), and limits the efficiency of the measurement chain to $\eta_\mu = 1/(1 + 2\bar{n})$. For a typical experiment operating at $|\alpha|^2 \approx n_{crit}/5 \approx 10$, with $\kappa/2\pi = 10$ MHz, $Z = 50$ Ω and $\omega/2\pi = 6$ GHz, one obtains $\bar{I} \approx 7$ nA and $\bar{n} \approx 0.03$. This leads to a microwave measurement efficiency limited to $\eta_\mu \approx 94\%$, much larger

than the state-of-the-art. Additionally, qubit measurement infidelity is typically dominated by qubit relaxation events during the measurement with only a small contribution due to the limited measurement efficiency[28]. We expect therefore that the assignment errors due to the photocurrent shot noise will be negligible.

Qubit control. We assume a qubit gate error rate dominated by the relaxation rate, $\Gamma_\downarrow$, and the excitation rate, $\Gamma_\uparrow$, which are linked by the detailed balance $\Gamma_\uparrow = \bar{n}\Gamma_\downarrow$. The error probability ϵ for a gate of length τ is:

$$\epsilon = 1 - \exp[-(\Gamma_\uparrow + \Gamma_\downarrow)\tau] = 1 - \exp[-(1+\bar{n})\Gamma_\downarrow\tau]. \quad (6)$$

For a π pulse at a Rabi rate $\Omega_R \gg (1+\bar{n})\Gamma_\downarrow$, the error probability becomes:

$$\epsilon = \frac{\pi\Gamma_\downarrow}{\Omega_R}(1+\bar{n}). \quad (7)$$

We decompose the qubit relaxation rate into an external contribution from the coupling to the control line, Γ_{ext}, and an internal contribution from all other degrees of freedom, Γ_{int}. The Rabi rate is defined as $\Omega_R = 2\sqrt{\dot{n}\Gamma_{ext}}$ where $\dot{n}$ is the photon flux in photon/s at the control line. The effective qubit population, $\bar{n}$, is linked to the population of the internal and external bath, $\bar{n}_{int}$ and $\bar{n}_{ext}$, by detailed balance so that $\Gamma_\downarrow\bar{n} = \Gamma_{int}\bar{n}_{int} + \Gamma_{ext}\bar{n}_{ext}$. In the following we will assume that the internal bath is cold, $\bar{n}_{int} = 0$.

For a photodiode operating well within its bandwidth driving a control line of impedance Z, the photon flux is set by the microwave power generated by the photodiode $\hbar\omega_q\dot{n} = \frac{1}{2}Z\bar{I}^2$, and the external bath occupancy is set by the photon shot noise $\hbar\omega_q\bar{n}_{ext} = 2e\bar{I}Z$, leading to:

$$\epsilon = \frac{\pi}{\sqrt{2}}\left(\frac{\Gamma_\downarrow}{\bar{I}}\sqrt{\frac{\Lambda}{\Gamma_{ext}}} + 2e\sqrt{\frac{\Gamma_{ext}}{\Lambda}}\right). \quad (8)$$

At low photocurrent, $\bar{I} \ll \hbar\omega_q\Gamma_\downarrow/(2eZ\Gamma_{ext})$, the microwave noise generated by the photodiode is negligible, $\bar{n} \ll 1$. In this regime the error probability decreases as the ratio between Rabi rate and relaxation rate increases. By contrast, at high photocurrent, $\bar{I} \gg \hbar\omega_q\Gamma_\downarrow/(2eZ\Gamma_{ext})$, the error probability plateaus as the errors induced by the photocurrent shot noise balances the increase in Rabi rate. For a realistic case where $\omega_q/2\pi = 6$ GHz, $Z = 50\ \Omega$ and $1/\Gamma_{ext} = 1$ ms, the error probability saturates at $\epsilon = 8 \times 10^{-5}$, far below what has been achieved in state-of-the-art-systems. As the drive line impedance increases the error probability saturates at lower photocurrent, but to a higher value ($\epsilon = 10^{-3}$ for $Z = 10$ kΩ). Note that as qubit coherence improves, the coupling rate to the control line will have to decrease to maintain $\Gamma_{ext} \ll \Gamma_\downarrow$, which reduces the minimum error probability at high photocurrent (see equation (8) for $\bar{I} \gg \hbar\omega_q\Gamma_\downarrow/(2eZ\Gamma_{ext})$).

Finally, we note that the spectrum of microwave noise induced by the photocurrent shot noise on the photodiode is white up to the bandwidth of the photodiode. Consequently, when considering an architecture where multiple qubits are addressed using a single photodiode, one would have to take into account that driving one qubit will subject all the other qubits to the microwave white noise of the photodiode.

Heat load estimation

Here we detail the calculations and assumptions used to estimate and compare the heat load of the regular coaxial approach and the photonic link approach. For simplicity, we focus on the heat load associated with the qubit microwave control lines, and neglect here all other heat loads, such as those associated with qubit readout and d.c.-flux biasing. For both approaches, the heat can be divided into a passive and active heat load. The passive heat load is set by the heat flow through the coaxial cables or optical fibres. The active heat load comes from the Joule heating in the attenuators in the coaxial approach and from the dissipated optical power in the photonic link approach.

Passive heat load. Previous work has investigated the heat load for the coaxial line approach[5]. We focus here on the heat load on the mixing chamber of a dilution refrigerator from the 100-mK stage. Although the heat load from a 0.086-inch (2.2-mm) diameter stainless steel coaxial cable is calculated to be 4 nW, a larger value of $P_{coax} = 13$ nW has been measured[5]. In theory, using thinner cables should reduce the heat load as the square of the diameter, but systematic measurements of the performance of these cables have yet to be conducted. In comparison, we estimate the heat load of an optical fibre to be orders of magnitude smaller, at $P_{link} = 3$ pW. We assumed a silica core and cladding of 125-μm diameter with a coating increasing the diameter to 250 μm. In the absence of data about the thermal conductivity of the coating at low temperature, we assume it is the same as silica, which was measured down to 100 mK (ref. [35]).

Active heat load. The microwave power required at the qubit control line, $P(t) = \hbar\omega_q\dot{n}(t)$, depends on the Rabi rate and coupling rate so that $P(t) = \hbar\omega_q\Omega_R(t)^2/4\Gamma_{ext}$ where $\Omega_R(t) = \Omega_R S(t)$ and $S(t)$ is the time domain pulse shape. We define the average power of a pulse of duration τ as $\bar{P} = \int_0^\tau P(t)/\tau = \hbar\omega_q\Omega_R^2\bar{S}^2/4\Gamma_{ext}$ with $\bar{S} = \int_0^\tau S(t)/\tau$.

In the coaxial approach, attenuation at the mixing chamber is necessary to reduce the black body radiation from higher temperature stages. This leads to an active heat load per control pulse $P^{act}_{coax} = \bar{P} \times (1/A - 1)$ where $A < 1$ is the attenuation.

In the photonic link approach, the optical power is fully dissipated as heat, leading to an active heat load per control pulse $P^{act}_{link} = \sqrt{2\bar{P}/\mathcal{Z}\mathcal{R}^2}$, neglecting loss between the photodiode and the control line.

Total heat load. The total heat load strongly depends on the duty cycle per qubit D, $P_{coax,link} = P^{pass}_{coax,link} + D \times P^{act}_{coax,link}$ The total number of qubits that can be addressed in both approaches is $N_{coax,link} = P_{cool}/P_{coax,link}$ where P_{cool} is the cooling power at the mixing chamber.

In Fig. 4 we use the following parameters: $\Gamma_{ext} = 1\,\mathrm{ms}^{-1}$, $\Omega_R/2\pi = 40$ MHz, $\mathcal{R} = 1\,\mathrm{AW}^{-1}$, $\omega_q/2\pi = 6$ GHz, $P_{cool} = 20$ μW, $P_{coax} = 13$ nW, $P_{link} = 3$ pW, $A = 0.01$ and $S(t)$ is a $\cos^2$ pulse shape leading to $\bar{S} = 0.5$.

Experimental details

A detailed experimental diagram is available in Extended Data Figs. 4, 5. High-efficiency qubit readout is enabled by the use of a low-noise parametric microwave amplifier, based on a field-programmable Josephson amplifier (FPJA)[42], followed by a high-electron-mobility transistor amplifier (HEMT). A summary of the various device parameters is shown in Table 1.

Photonic link. The photodetector used here is a commercially available, high-speed photodiode with an InGaAs absorber, packaged with a fibre pigtail[43]. We note that previous experiments[6] with a surface illuminated modified unitravelling carrier (MUTC) InGaAs photodiode also successfully generated microwave signals at 20 mK. We would expect MUTC detectors, and probably many others, to exhibit similar overall performance as the commercial detector used in this experiment. Owing to the bandgap shift of InGaAs as the photodiode is cooled[44], it is illuminated at a wavelength of 1,490 nm. An external bias tee was used to monitor the d.c. photocurrent and apply a voltage bias. For the qubit readout experiment (Figs. 2b, c, 3a), no bias voltage was applied. For the qubit control experiment (Figs. 2e, f, 3b), a voltage of −2 V was applied. In Extended Data Fig. 2 we show the photodiode *IV* curve at 20 mK in absence of optical power.

The optical set-up at room temperature uses a commercial semiconductor distributed-feedback 1,490 nm laser. The intensity of the laser was modulated by an external $LiNbO_3$ Mach–Zehnder EOM. A second

EOM, followed by a mechanical attenuator, is used to finely control the average optical power and ensure a power on/off ratio in excess of 30 dB. Note that EOMs with extinction ratios in excess of 50 dB are commercially available.

Similar to any photonic link used for telecommunication applications at room temperature, the photonic link used here allows for full vector control of the microwave signal. We confirm the control over the microwave phase by using the photonic link to drive a Ramsey sequence where the phase of the second pulse is varied, showing good agreement with theory (Extended Data Fig. 3).

In general, the nonlinearity of a microwave photonic link can result in spurious tones. The dominant nonlinearity of a Mach–Zehnder-style EOM biased at its quadrature point leads to third-harmonic generation, which is outside the bandwidth of our system for both control and readout microwave frequencies. The photodetector can produce harmonic distortion, and mixing products may be produced when photodetecting multiplexed microwave signals. Careful measurement of the nonlinear mixing products of a similar photodiode operated at cryogenic temperature was previously reported[6], where a spur-free dynamic range >60 dB for second- and third-order nonlinearities was demonstrated. We note that predistortion of the microwave signals can mitigate these nonlinear effects, but it was not necessary in this experiment.

Qubit fabrication. The transmon qubit was fabricated using standard optical and electron beam lithography techniques on a sapphire substrate. A sputtered and patterned Nb film forms capacitor electrodes, and a shadow-evaporated Al–AlO_x–Al Josephson junction is produced using the Dolan resist bridge technique. An additional evaporated Al 'patch' layer connects the junction electrodes to the Nb capacitor pads that previously had its native oxides removed by an Ar ion-mill step. The qubit chip was then placed into a machined three-dimensional Al cavity.

Qubit coherence. In general, transmon relaxation rates vary as a function of time and are best characterized by their distributions. In Extended Data Fig. 1 we compare histograms of the qubit relaxation time measured either in the absence of light on the photodiode or with approximately 2 μW of optical power, using the set-up from Fig. 2a (readout experiment). Both distributions yield an average relaxation time of $T_1 \approx 43$ μs, with no statistically relevant differences. The same relaxation time was measured using the set-up from Fig. 2d (control experiment).

The Ramsey oscillations shown in Fig. 2c are representative of a set of five Ramsey oscillations performed with both the coaxial line and the photonic link, yielding the coherence times of (31, 34, 37, 40, 43) μs and (36, 36, 37, 38, 42) μs, respectively.

Qubit and cavity thermal occupancy. In Fig. 3a we measure a background cavity occupancy of about 1%, corresponding to an effective temperature $T_{\mathrm{eff}} = 115$ mK at $\omega_c/2\pi = 10.866$ GHz. In Fig. 3b we measure a background qubit occupancy of about 10%, corresponding to an effective temperature $T_{\mathrm{eff}} = 100$ mK at $\omega_q/2\pi = 5.088$ GHz. These occupancies, typical in our system, could probably be reduced by increasing attenuator thermalization[45,46], line filtering[47] and device shielding[48]. We emphasize, however, that these occupancies have been verified over several cooldowns to be independent of whether or not the photodiode is connected.

Data availability

The experimental data and numerical simulations presented here are available from the corresponding authors upon request.

36. Gambetta, J. et al. Quantum trajectory approach to circuit QED: quantum jumps and the Zeno effect. *Phys. Rev. A* **77**, 012112 (2008).
37. Clerk, A. A. & Utami, D. W. Using a qubit to measure photon-number statistics of a driven thermal oscillator. *Phys. Rev. A* **75**, 042302 (2007).
38. Houck, A. A. et al. Controlling the spontaneous emission of a superconducting transmon qubit. *Phys. Rev. Lett*. **101**, 080502 (2008).
39. Nigg, S. E. et al. Black-box superconducting circuit quantization. *Phys. Rev. Lett*. **108**, 240502 (2012).
40. Boyd, R. W. *Radiometry and the Detection of Optical Radiation* (Wiley, 1983).
41. Yariv, A. & Yeh, P. *Photonics: Optical Electronics in Modern Communications* 5th edn (Oxford Univ. Press, 1997).
42. Lecocq, F. et al. Nonreciprocal microwave signal processing with a field-programmable Josephson amplifier. *Phys. Rev. Appl*. **7**, 024028 (2017).
43. W. Liu, R. Cendejas, H. Cao, Q. Hang, Z. Ji, and A. Nikolov, Uncooled low-bias uni-traveling carrier photodetectors. In *2013 Conf. Lasers and Electro-Optics (CLEO) Science and Innovations* OSA Technical Digest CTh3L.2 (OSA 2013).
44. Zielinski, E., Schweizer, H., Streubel, K., Eisele, H. & Weimann, G. Excitonic transitions and exciton damping processes in InGaAs/InP. *J. Appl. Phys*. **59**, 2196 (1986).
45. Yeh, J.-H., LeFebvre, J., Premaratne, S., Wellstood, F. C. & Palmer, B. S. Microwave attenuators for use with quantum devices below 100 mK. *J. Appl. Phys*. **121**, 224501 (2017).
46. Wang, Z. et al. Cavity attenuators for superconducting qubits. *Phys. Rev. Appl*. **11**, 014031 (2019).
47. Serniak, K. et al. Direct dispersive monitoring of charge parity in offset-charge-sensitive transmons. *Phys. Rev. Appl*. **12**, 014052 (2019).
48. Córcoles, A. D. et al. Protecting superconducting qubits from radiation. *Appl. Phys. Lett*. **99**, 181906 (2011).

Acknowledgements We thank J. Davila-Rodriguez, J. Campbell and E. Ivanov for early contributions to this work. We thank S. W. Nam and K. Lehnert for comments on the manuscript. This work was supported by the NIST Quantum Information Program.

Author contributions F.L., F.Q., J.A., S.A.D. and J.D.T. conceived and designed the experiment. F.L., F.Q. and J.D.T. built the experimental set-up. F.L. performed the experiment and F.L., F.Q. and J.D.T. analysed the data. K.C. fabricated the transmon qubit. All authors contributed to the manuscript.

Competing interests The authors declare no competing interests.

Additional information
Correspondence and requests for materials should be addressed to F.L., F.Q. or J.D.T.

Peer review information *Nature* thanks Joseph Bardin, Blake Johnson and the other, anonymous, reviewer(s) for their contribution to the peer review of this work.

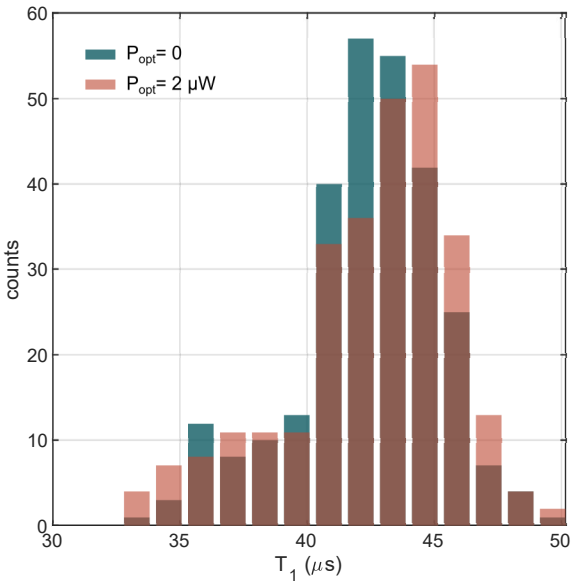

Extended Data Fig. 1 | Relaxation time in the presence of optical light. Histogram of 280 measurements of the relaxation time of the qubit with 2 μW of optical power applied to the photodiode during the qubit evolution. Comparison with data in the absence of optical power confirm that the qubit relaxation time is not affected by stray optical photons, with an average relaxation time $T_1 \approx 43$ μs. Data were acquired using the set-up in Fig. 2a.

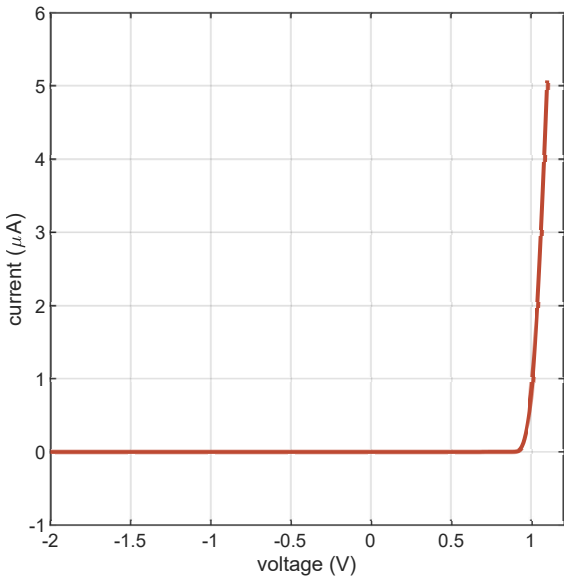

Extended Data Fig. 2 | Photodiode current–voltage characteristic. Measured d.c. current through the photodiode as a function of voltage bias, in the absence of optical power. The dark current is below the 10-pA resolution of the current meter.

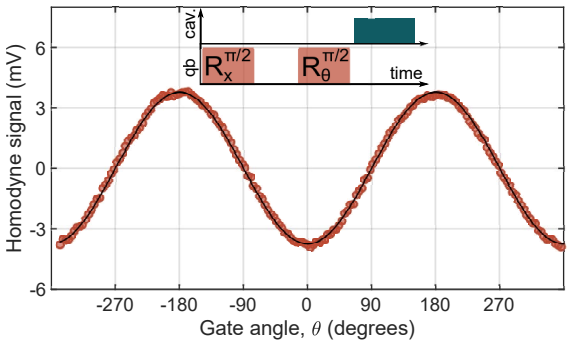

Extended Data Fig. 3 | Vector control with the photonic link. Ramsey oscillation driven by the photonic link, as a function of the phase θ of the second π/2 pulse (same set-up as Fig. 2d). Data (dots) follow a clean sinusoidal dependence (line). $R_x^{\pi/2}$ denotes a π/2 qubit rotation around the x axis and $R_\theta^{\pi/2}$ denotes a π/2 qubit rotation around an axis with a variable angle θ within the x–y plane. qb, qubit; cav., cavity.

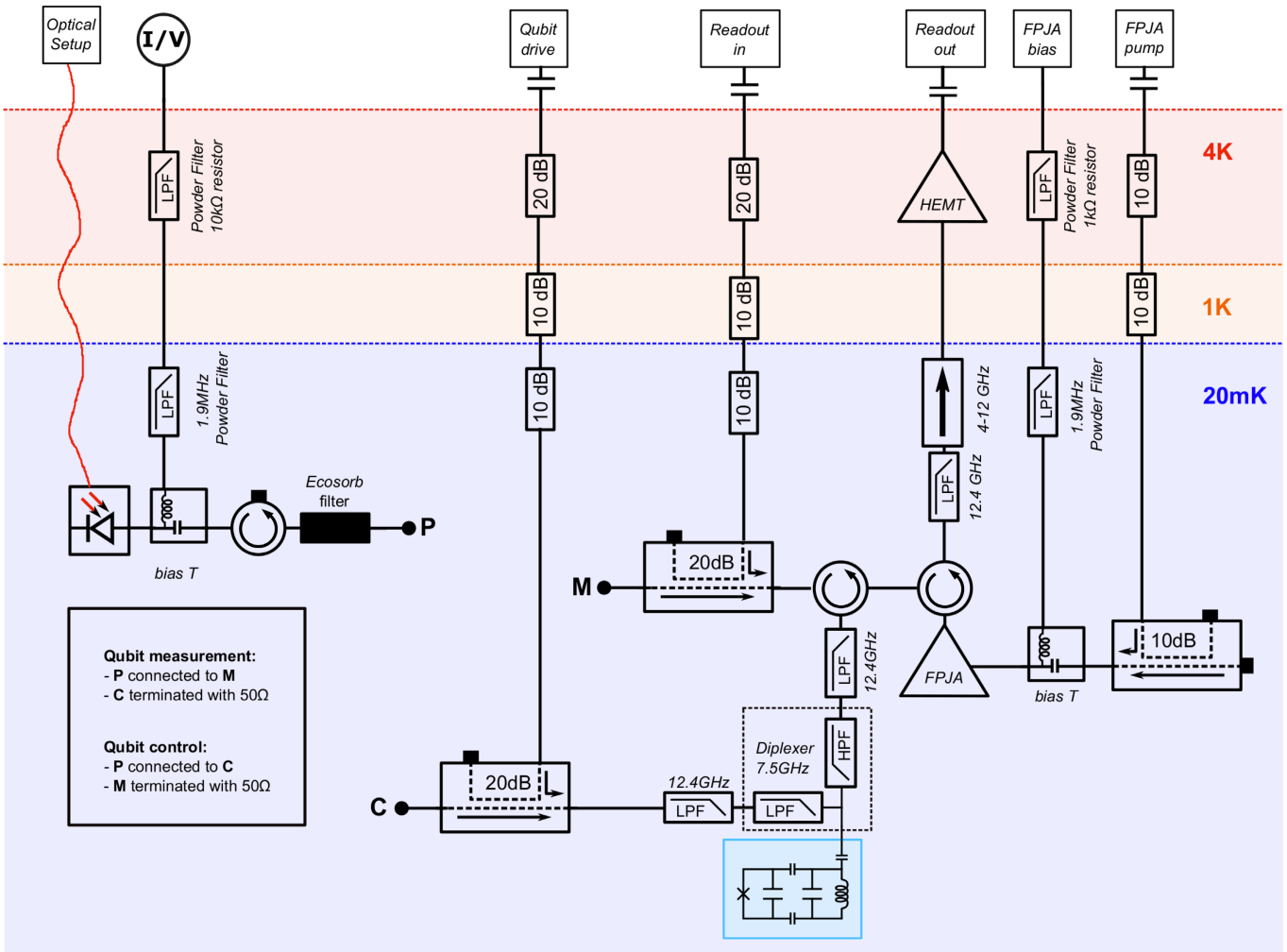

Extended Data Fig. 4 | Dilution refrigerator wiring. Details of the circuitry employed in the cryostat for qubit measurement and control experiments. The qubit cavity device is placed inside a double layer cryoperm shield. FPJA, field-programmable Josephson amplifier (see text); HEMT, high-electron-mobility transistor amplifier, LPF, low-pass filter.

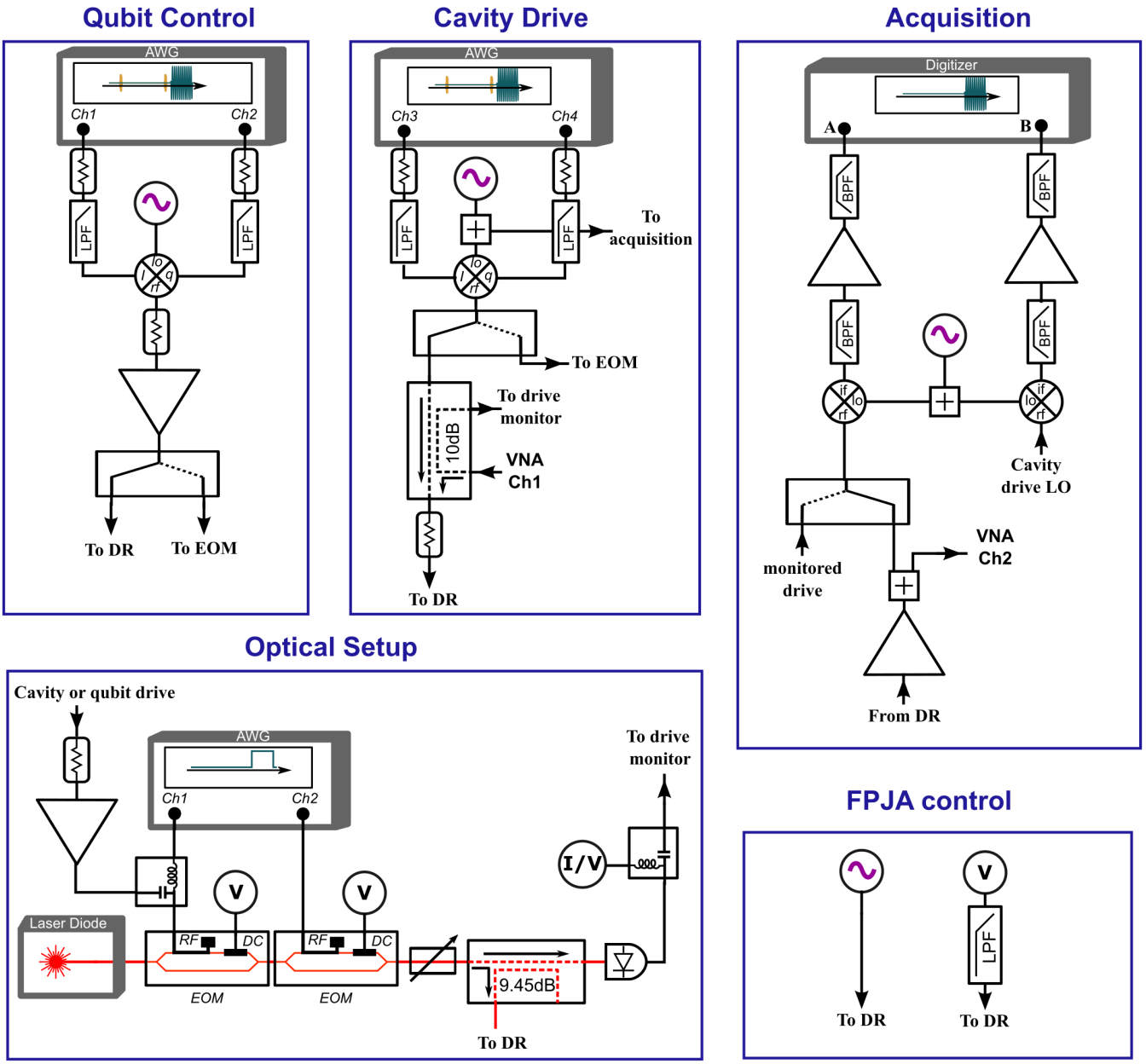

Extended Data Fig. 5 | Simplified room-temperature set-up. The FPJA pump, cavity local oscillator (LO) and demodulation LO share a 1-GHz reference clock and are locked to all other instruments via a 10-MHz reference clock. A master trigger, not shown, is shared via a distribution amplifier. There are slight differences in the set-up between the qubit control and measurement experiments. Amplification and attenuation levels are slightly different. The FPJA pump is pulsed on only during the qubit measurement. AWG, arbitrary waveform generator; BPF, band-pass filter; DR, dilution refrigerator; LPF, low-pass filter; VNA, vector network analyser.